



Article

Ocean Variability in the Costa Rica Thermal Dome Region from 2012 to 2021

Wei Shi ^{1,2,*} and Menghua Wang ¹

¹ National Oceanic and Atmospheric Administration, National Environmental Satellite, Data, and Information Service, Center for Satellite Applications and Research, College Park, MD 20740, USA; menghua.wang@noaa.gov

² Cooperative Institute for Research in the Atmosphere, Colorado State University, Fort Collins, CO 80523, USA

* Correspondence: wei.1.shi@noaa.gov

Abstract: Satellite ocean color and sea surface temperature (SST) observations from 2012 to 2021 and sea surface salinity (SSS) measurements from the Soil Moisture Active Passive (SMAP) mission from 2015 to 2021 are used to characterize and quantify the seasonal and interannual variability in the physical, optical, and biological sea surface features in the Costa Rica Thermal Dome (CRTD) region. High-resolution climatology and the seasonal variability in SST, SSS, and ocean color properties are produced. Chlorophyll-a (Chl-a) concentration, SST, and SSS show these three properties are linked with similar spatial patterns and seasonal variations, i.e., elevated Chl-a concentrations, match the depressed SST and increased SSS and vice versa. This reflects that the physical driving force is the same for these three ocean properties and implies that nutrient supply associated with the physical processes is the major driver for the seasonal biological variability. The interannual changes in Chl-a, SST, and SSS also show that these three ocean properties are consistent among themselves. The positive (negative) Chl-a anomaly generally occurs with negative (positive) SST anomaly and enhanced (reduced) SSS. The in situ measurements evidently show that the subsurface ocean dynamics in the upper 100 m controls the sea surface variability for Chl-a, SST, and SSS. We report that no significant enhancement of Chl-a is observed in the CRTD region during the central Pacific (CP)-type 2020–2021 La Niña event, while Chl-a changes are significant in the other three of four ENSO events between 2012 and 2021. Furthermore, the difference in Chl-a variability driven by the CP-type ENSO and eastern Pacific (EP)-type ENSO is further discussed.

Keywords: Costa Rica Thermal Dome (CRTD); satellite ocean color; chlorophyll-a; sea surface temperature; sea surface salinity; La Niña; El Niño; VIIRS; SMAP



Citation: Shi, W.; Wang, M. Ocean Variability in the Costa Rica Thermal Dome Region from 2012 to 2021.

Remote Sens. **2024**, *16*, 1340.

<https://doi.org/10.3390/rs16081340>

Academic Editors: Matteo Postacchini, Giovanni Ludeno, Giacomo De Carolis, Gianfranco Fornaro, Virginia Zamparelli, Sedat Gündoğdu and Ali Rıza Kosker

Received: 8 March 2024

Revised: 3 April 2024

Accepted: 8 April 2024

Published: 11 April 2024



Copyright: © 2024 by the authors. Licensee MDPI, Basel, Switzerland. This article is an open access article distributed under the terms and conditions of the Creative Commons Attribution (CC BY) license (<https://creativecommons.org/licenses/by/4.0/>).

1. Introduction

Located in the eastern tropical Pacific off the coast of Costa Rica, the Costa Rica Thermal Dome (CRTD) (Figure 1) [1,2] has a feature of the dome-like shoaling isotherm with a diameter varying from a couple of hundred km to ~1000 km. The CRTD is not only a region driven by a variety of the ocean and atmospheric processes but also a complex marine ecosystem with high nutrient concentration and ocean productivity, complicated chemical and biological processes, and significant biodiversity [3,4]. The environmental, economic, and societal importance of the CRTD to the nearby central American countries is also enormous.

The main physical driving force for the CRTD is the interaction of the trade winds with the three major currents in the eastern equatorial Pacific, i.e., the North Equatorial Countercurrent (NECC) [5–7], Costa Rica Coastal Current (CCCR) [8], and North Equatorial Current (NEC) [8,9]. Like most low-latitude domes, the CRTD is associated with the cyclonic turning of predominantly zonal tropical surface currents, i.e., NECC, CCCR, and NEC, as a geostrophic balance. The wind stress curl associated with the Intertropical Convergence Zone (ITCZ) plays an important role in generating the CRTD [10]. The

seasonal change in the CRTD is the response of the eastern tropical Pacific to meridional migration of the ITCZ. It grows rapidly in late spring and matures in summer and early fall in accordance with the northward migration of the ITCZ. The CRTD is eroded in winter and early spring by the westward-propagating warm anticyclones [11]. The annual cycle of the CRTD can be represented in four stages after analyzing the wind forcing, surface current, and structure and seasonal evolution of the dome [3].

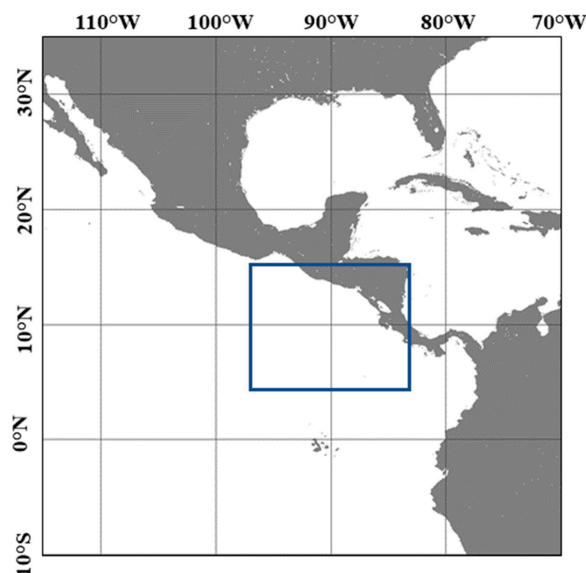


Figure 1. Blue box shows the study region of the Costa Rica Thermal Dome (CRTD).

The upwelling associated with the CRTD provides the nutrients from the deep-layer waters to the euphotic zone, and the dome in the open ocean supports high concentrations of chlorophyll-a (Chl-a) via the nutrient supply with upwelling [12]. The distribution of the nutrients and oxygen in the CRTD are mainly determined by the localized upwelling of nutrient-rich, oxygen-poor water from a depth of 65 m or deeper [13]. At a location of [8°35'N, 88°00'W], the nitrate concentration is usually ~6 µg/L at the surface and increases to ~29 µg/L at a 50 m depth. A similar profile is also found with the phosphate concentration.

The high concentrations of the nutrients lead to the growth of phytoplankton and high ocean productivity in the CRTD region and endow the region with a moderately high Chl-a concentration [14,15]. In fact, Chl-a in the CRTD region follows the cycle of the dome. The variability in the thermocline depth is strongly connected to the seasonal variability in surface Chl-a, and the surface Chl-a is also significantly affected by the El Niño Southern Oscillation (ENSO) variability [16] and Pacific Decadal Oscillation (PDO) [17]. On the other hand, nitrates are not depleted in the surface layer [15]. This may be attributed to various factors such as the low iron availability [15,17,18] and the balance of the production and the zooplankton grazing [19,20].

The complex physical dynamics, high nutrients, and high primary productivity nourish the CRTD to become one of the regions with the highest ecosystem biodiversity [4]. Indeed, zooplankton biomass is usually higher than that in the other equatorial upwelling regions [21]. The seasonal and spatial patterns of the zooplankton abundance follow the patterns of Chl-a and nutrients [3,22]. The Costa Rica cyclonic circulation surrounding the Costa Rica Dome is a hydrodynamic trap for the larvae of nearshore fish [23]. Indeed, fish in deep and intermediate depth waters such as dragonfish and lampfish are abundant in the CRTD. In fact, the CRTD and nearby regions are some of the largest tuna catch areas in the world [24]. The high biological productivity in the CRTD is the major reason for the high-density patches of the yellow tuna [25].

Satellite remote sensing has been used in a variety of studies in the CRTD region [3,14,16]. However, there is no synthetic study using satellite products, i.e., Chl-a, SST, and SSS,

to address the ocean features in the CRTD region. In this study, satellite ocean color measurements (2012–2021) from the Visible Infrared Imaging Radiometer Suite (VIIRS) onboard the Suomi National Polar-Orbiting Partnership (SNPP), SST from the NCEP Global Ocean Data Assimilation System (GODAS) [26,27] corresponding to the same VIIRS observation period, and SSS measurements from the Soil Moisture Active Passive (SMAP) mission [28] since April 2015 are used to characterize and quantify the physical, optical, and biological properties and their variability. The linkage of the ocean physical and biological processes is also explored. In particular, the ENSO impact on these ocean property features in the CRTD during this period is further assessed and discussed.

2. Data and Methods

The hydrography of CRTD can be represented using the shoaling thermocline depths. The climatology of the 20° isothermal depth in the eastern tropical Pacific (Figure 2a) shows that the core of the CRTD region stretches from 93°W to 87°W in longitude and 7°N to 11°N in latitude with the top of the dome at ~20 m located at about [89°W, 9°N]. Note that the climatology data are for the normal condition from multi-year average data. The low SST in the CRTD follows a similar pattern to the 20° isothermal depth, even though its core shifts a little bit to the north (Figure 2b). SST in the core CRTD is normally >1 °C lower than that in the neighboring region. The existence of the CRTD in the eastern tropical Pacific also results in enhanced SSS (Figure 2c). The pattern of the enhanced SSS is similar to that of the lower SST in Figure 2b. The climatology nitrate concentration at the sea surface also shows that it is enhanced in the CRTD region, even though the spatial pattern is different from the SST or SSS (Figure 2d). Note that the hydrography of the CRTD region is built on the historical in situ measurements which might be scarce in this region. Thus, it becomes necessary to use the most recent satellite measurements with much higher spatial and temporal resolutions in the CRTD region to characterize and quantify the variability in the physical, optical, and biological properties and their variability and assess the ocean physical and biological processes that drive these changes in the region.

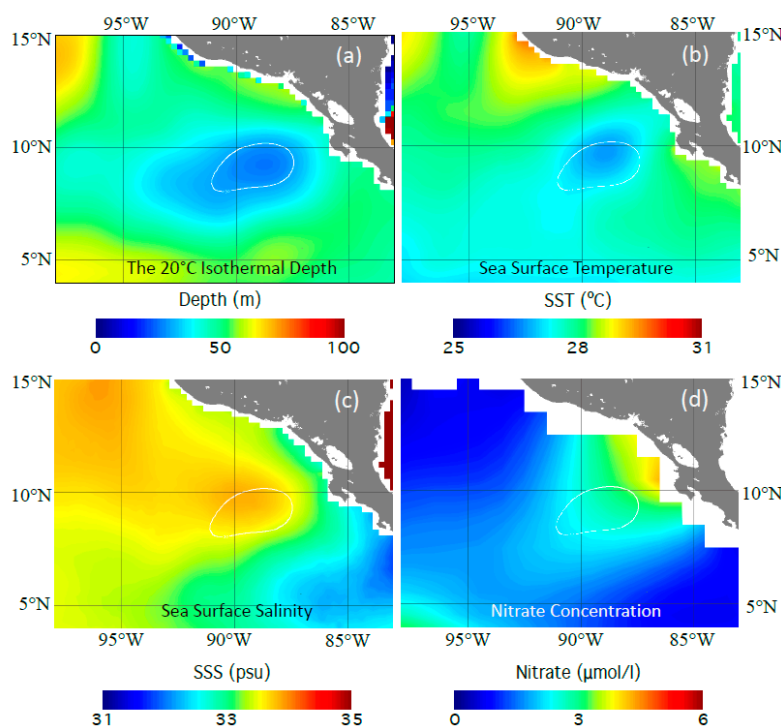


Figure 2. World Ocean Atlas 2018 (WOA2018) (<https://www.ncei.noaa.gov/access/world-ocean-atlas-2018/>; accessed on 10 April 2024) climatology of (a) the 20°C isothermal depth, (b) SST, (c) SSS, and (d) nitrate concentration in the CRTD region. White line in each panel represents the 30 m isothermal depth derived from the climatology temperature profiles in the region.

2.1. VIIRS Satellite Ocean Color Products

As a continuation mission for the Moderate Resolution Imaging Spectroradiometer (MODIS) onboard the Terra and Aqua satellites [29,30] to provide the satellite ocean color products for the global ocean, VIIRS-SNPP [31] has been providing high-quality satellite ocean products including normalized water-leaving radiance spectra $nL_w(\lambda)$ from the blue to the near-infrared (NIR) bands [32]. The VIIRS ocean color data have been routinely derived using the Multi-Sensor Level-1 to Level-2 (MSL12) ocean color data processing system [32]. The $nL_w(\lambda)$ spectra are derived from the satellite measured top-of-atmosphere (TOA) radiance after removing the Rayleigh (air molecules) and aerosol contributions using an NIR-based atmospheric correction scheme for the open ocean [33] and shortwave infrared (SWIR) atmospheric correction [34,35] for the coastal and inland waters. To produce high-quality global satellite ocean color products consistent with those from the previous satellite sensors such as the Sea-viewing Wide Field-of-view Sensor (SeaWiFS) and MODIS [36,37], the on-orbit vicarious calibration has been carried out for VIIRS using the in situ $nL_w(\lambda)$ measurements from the Marine Optical Buoy (MOBY) [38,39]. As the fundamental products in satellite ocean color remote sensing, high-quality $nL_w(\lambda)$ spectra from VIIRS-SNPP have been achieved for both the global open ocean and coastal/inland waters [40–42].

The VIIRS-SNPP Chl-a product is produced from the satellite measured $nL_w(\lambda)$. For oligotrophic waters, Chl-a is computed with a color index (CI)-based algorithm [43,44]. The blue-green $nL_w(\lambda)$ ratio algorithm [45,46] is used to compute Chl-a values for the other regions. These two algorithms are then merged as the ocean color index (OCI) algorithm to generate Chl-a products for the global open ocean and coastal/inland waters [44]. In this study, the VIIRS-SNPP-derived monthly $nL_w(\lambda)$ spectra and Chl-a are used to study the seasonal climatology and interannual variability in the ocean optical and biological features in the CRTD region. The ENSO impact on the biological activities in the region is also evaluated with VIIRS-SNPP measurements.

2.2. SST and SSS Data

As the most important physical property for oceans, SST data corresponding to the VIIRS observation period in this study are the output of the NCEP Global Ocean Data Assimilation System (GODAS) [26,27]. GODAS is a real-time ocean analysis and a reanalysis. The SST data have a spatial resolution of $1/3 \times 1/3$ degrees. Evaluation results show that the output of the GODAS matched well with in situ ocean observations [47,48].

There has been no previous study characterizing and quantifying SSS variability with satellite remote sensing in the CRTD region. Most of our knowledge about SSS is from various in situ measurements and the climatology data, as shown in Figure 2c. The SMAP mission [28] is to measure the amount of water in the surface soil everywhere on Earth. It also provides SSS observations from its radar and radiometers based on the L-band microwave sensitivity to water salinity [49,50]. The spatial resolution of SMAP is 25 km on the swath grid and $0.25^\circ \times 0.25^\circ$ for L3 data. The accuracy of the SMAP SSS is better than 0.2 psu in comparison to the objectively interpolated (OI) gridded monthly Argo datasets in the tropics [51]. In this study, the SMAP SSS data in the CRTD region starting from April 2015 are used to characterize and quantify the seasonal and interannual features of SSS. Both SST and SSS are analyzed together with the satellite ocean color data to provide a comprehensive view and understanding of the physical, optical, biological, and biogeochemical processes in the CRTD region.

2.3. In Situ Data

Even though satellite remote sensing can provide a broad assessment of the sea surface features related to the CRTD, it is difficult to further assess the ocean processes that drive the sea surface property without the in situ ocean profile measurements such as the temperature and salinity profiles. As the array of moorings buoy across the tropical Pacific Ocean, Tropical Atmosphere and Ocean (TAO) is the ocean observing system to support the

seasonal-to-interannual climate studies with in situ measurements of the ocean parameters such as temperature, salinity, winds, currents, etc. [52,53]. About 70 moorings span from 95°W near the Galapagos Islands to 137°E off the coast of New Guinea, separated by 10–15 degrees of longitude and 2–3 degrees of latitude between 8°N and 8°S. These ocean and atmospheric parameters are measured on a daily basis. The in situ measurements at some TAO stations could go back to the 1970s. In this study, we use in situ measurements taken at the location [95°W, 8°N] to investigate the interannual variability in SSS, SST, and Chl-a between 2015 and 2018 in the CRTD region.

3. Results

3.1. Climatology of $nL_w(\lambda)$, Chl-a, SST, and SSS

To study the ocean variability in the CRTD region, the long-term climatology and seasonal climatology of ocean properties, i.e., Chl-a, SST, and SSS, are computed. Specifically, the climatology of Chl-a and SST are computed as the mathematical mean values of all the observations between 2012 and 2021 in the CRTD region, and SMAP SSS climatology is the mean SSS between April 2015 and 2021 since SMAP launches in the corresponding months and seasons. Similarly, the seasonal and monthly climatology of Chl-a, SST, and SSS are computed in the same time range. Note that the climatology of Chl-a, SST, and SSS derived in this study are different from those of the WOA2018 which are solely based on the sparse in situ measurements in this region, as shown in Figure 2.

In the CRTD region, all the physical, optical, and biological properties show important influences. For optical properties, the $nL_w(443)$ values in the CRTD are lower than those in the neighboring regions. In the center of the CRTD, the $nL_w(443)$ values are $\sim 0.7\text{--}0.8 \text{ mW cm}^{-2} \mu\text{m}^{-1} \text{ sr}^{-1}$, while the $nL_w(443)$ values in the neighboring regions reach over $\sim 1.2 \text{ mW cm}^{-2} \mu\text{m}^{-1} \text{ sr}^{-1}$ (Figure 3a). In comparison, moderately enhanced $nL_w(551)$ (Figure 3b) and $nL_w(671)$ (Figure 3c) are also found in the CRTD region.

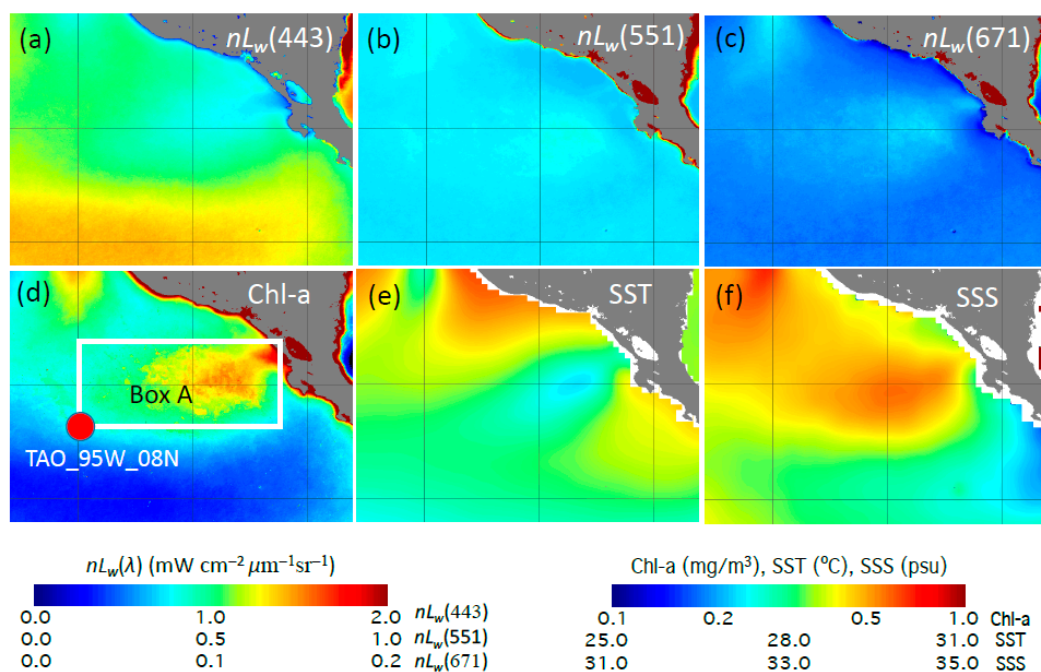


Figure 3. Climatology of sea surface properties in the CRTD region from 2012 to 2021 for (a) normalized water-leaving radiance $nL_w(443)$, (b) $nL_w(551)$, (c) $nL_w(671)$, (d) Chl-a, (e) SST, and (f) SSS. Note that Box A (95.0°W–86°W, 8°N–12°N) and station TAO_95W_08N at [95.0°W, 8°N] are marked in (d) for further data analysis.

The enhancement of climatology Chl-a is significant in the CRTD region (Figure 3d). In the core of the CRTD, Chl-a reaches $\sim 0.4\text{--}0.5 \text{ mg/m}^3$. This is significantly higher than

Chl-*a* in the southern region where its value ranges $\sim 0.1\text{--}0.2\text{ mg/m}^3$. The SST field shows the lower SST in the CRTD region (Figure 3e) generally match SST from the climatology SST from all the in situ observations in this region, as shown in Figure 2b, in terms of both the location of the dome and the magnitude of SST. The impact of the CRTD on SSS is also significant (Figure 3f). The enhancement of the SSS is over ~ 0.5 psu.

3.2. Seasonal Variability in $nL_w(\lambda)$, Chl-*a*, SST, and SSS

Figure 4 shows the seasonal variability in $nL_w(\lambda)$ at 443 nm (Figure 4a–d), 551 nm (Figure 4e–h), and 671 nm (Figure 4i–l). Over the four seasons, changes in $nL_w(\lambda)$ at these three bands are remarkable. The depression of $nL_w(443)$ is more enhanced in the spring (Figure 4a) and winter (Figure 4d) seasons, while $nL_w(551)$ values are more enhanced in spring (Figure 4e) and summer (Figure 4f). In winter, no significant enhancement of $nL_w(551)$ can be observed (Figure 4h). For $nL_w(671)$, the seasonal change is similar to that of $nL_w(551)$, i.e., strengthened $nL_w(671)$ in spring (Figure 4i) and summer (Figure 4j) and weakened $nL_w(671)$ (Figure 4l) in winter.

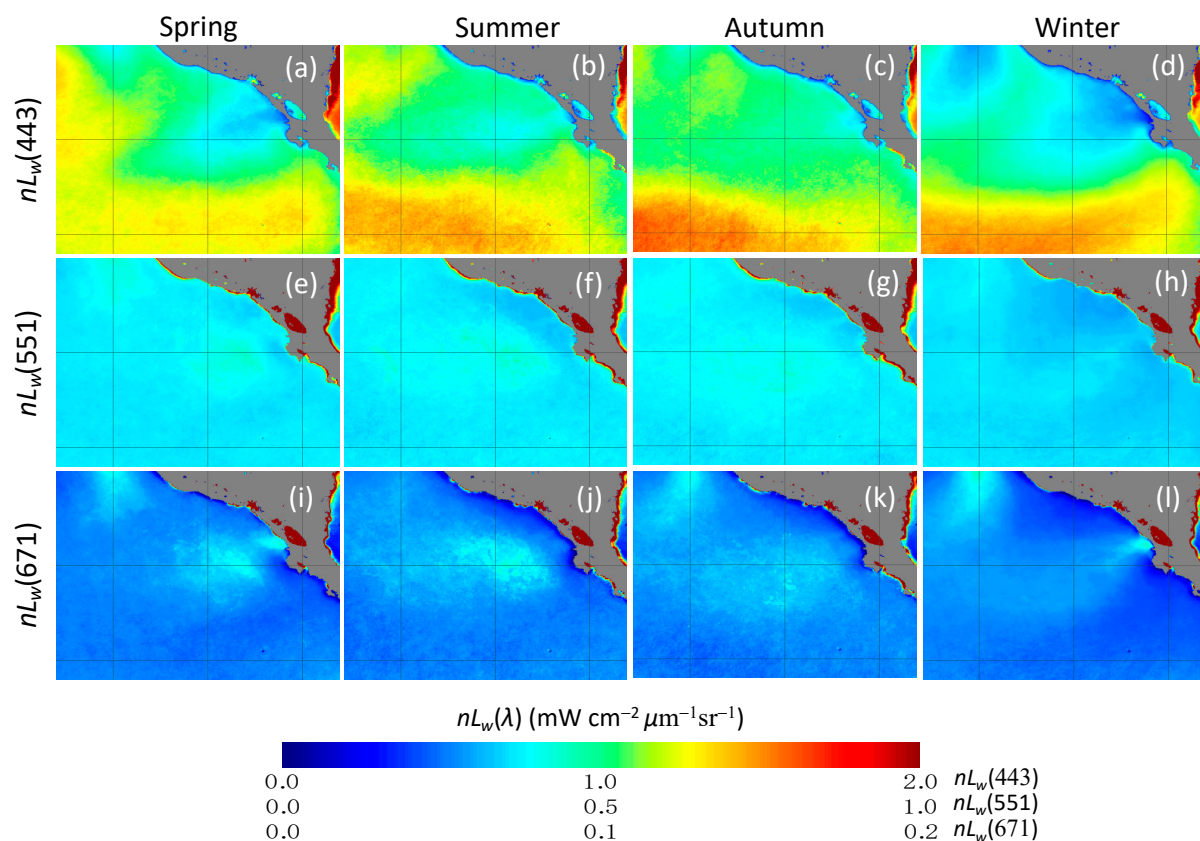


Figure 4. Seasonal images between 2012 and 2021 in the CRTD region during boreal spring (March–May), summer (June–August), autumn (September–November), and winter (December–February) for (a–d) $nL_w(443)$, (e–h) $nL_w(551)$, and (i–l) $nL_w(671)$.

The seasonal Chl-*a* change essentially reflects the seasonal spectral change in $nL_w(\lambda)$ since satellite-derived Chl-*a* values are computed from $nL_w(\lambda)$ spectra in visible bands. In general, the CRTD region features elevated Chl-*a* in comparison with that of the neighboring regions. As shown in Figure 5a–d, elevated Chl-*a* can be found in spring (Figure 5a), summer (Figure 5b), and winter (Figure 5d), while the elevation of Chl-*a* in autumn (Figure 5c) is less pronounced. On the other hand, the spatial patterns, coverage, and the core locations of the elevated Chl-*a* are different in different season. This implies that the CRTD is not only highly dynamic in terms of the thermocline depth but also has high seasonal variability in the biological activity that is driven by the physical forcing.

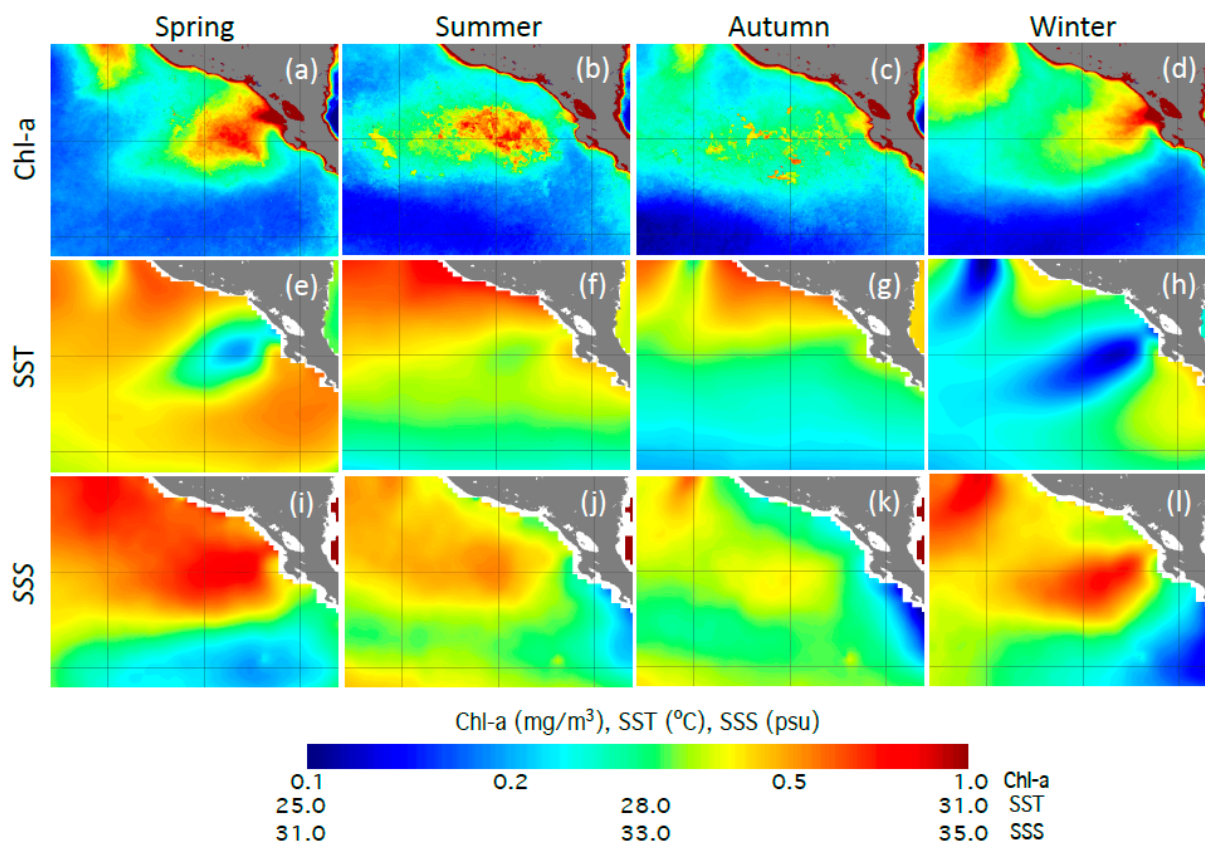


Figure 5. Seasonal climatology images between 2012 and 2021 in the CRTD region during boreal spring (March–May), summer (June–August), autumn (September–November), and winter (December–February) for (a–d) Chl-a, (e–h) SST, and (i–l) SSS.

The seasonal change in SST in the CRTD region is also significant. This is especially true in spring (Figure 5e) and winter (Figure 5h). The SST values in the CRTD region are generally about 2 °C lower than those in the nearby regions during winter. In fact, the low SST pattern stretches over 1000 km offshore (Figure 5h). In summer, the low SST pattern in the CRTD region is less significant (Figure 5f). It even becomes invisible during autumn (Figure 5g). This can be attributed to the migration of the ITCZ and erosion of the CRTD due to the strong air–sea interaction and heat exchange in this season.

SSS in the CRTD also shows high seasonal variability. Contrary to SST, SSS is found to be the highest in spring (Figure 5i) and winter (Figure 5l). As an example, the SSS values in the core CRTD region are ~35 psu in spring, while they are only ~33 psu to the south of the CRTD region. In summer, the SSS values in the CRTD region are about 0.5 psu higher than those in the neighboring regions, and the location and pattern of the moderately enhanced SSS (Figure 5i) generally match with the location and pattern of the lower SST (Figure 5e). In autumn, a slightly higher SSS pattern associated with the CRTD is found further offshore (Figure 5k).

3.3. Interannual Variability in Chl-a, SST, and SSS

To study the interannual variability in Chl-a, SST, and SSS, Box A (95.0°W–86°W, 8°N–12°N), as shown in Figure 3d, is set to cover the main CRTD region, and the time series of Chl-a, SST, and SSS are computed to evaluate the interannual variability between 2012 and 2021. In addition, we also compute the mean monthly values of Chl-a, SST, and SSS between 2012 and 2021 in the box as the Chl-a, SST, and SSS climatology references. These monthly Chl-a, SST, and SSS values are compared with the climatology values of Chl-a, SST, and SSS in each month to further address the interannual changes in Chl-a, SST, and SSS and the covariations and correlations of these properties.

In Box A, the mean monthly climatology Chl-a values generally vary between 0.266 mg/m^3 in June and 0.353 mg/m^3 in March (Figure 6a). This Chl-a seasonal variation in Box A is consistent with that of the entire CRTD region in Figure 5a–d. In comparison with the climatology seasonal variability, the interannual variability in the monthly Chl-a in Box A is significant, ranging from $<0.2 \text{ mg/m}^3$ to $\sim 0.6 \text{ mg/m}^3$. Specifically, the monthly Chl-a in 2013 was $\sim 0.2\text{--}0.4 \text{ mg/m}^3$ higher than the 10-year mean climatology Chl-a in the corresponding months. The ratios of the monthly Chl-a and the corresponding 10-year monthly mean Chl-a reach over 2. On the contrary, in the period between the spring of 2015 and the spring of 2016, the Chl-a values in Box A were only about 50% of the 10-year mean Chl-a in the corresponding months. In the period of 2019–2020, the Chl-a values in Box A were also significantly lower than the corresponding 10-year monthly mean values.

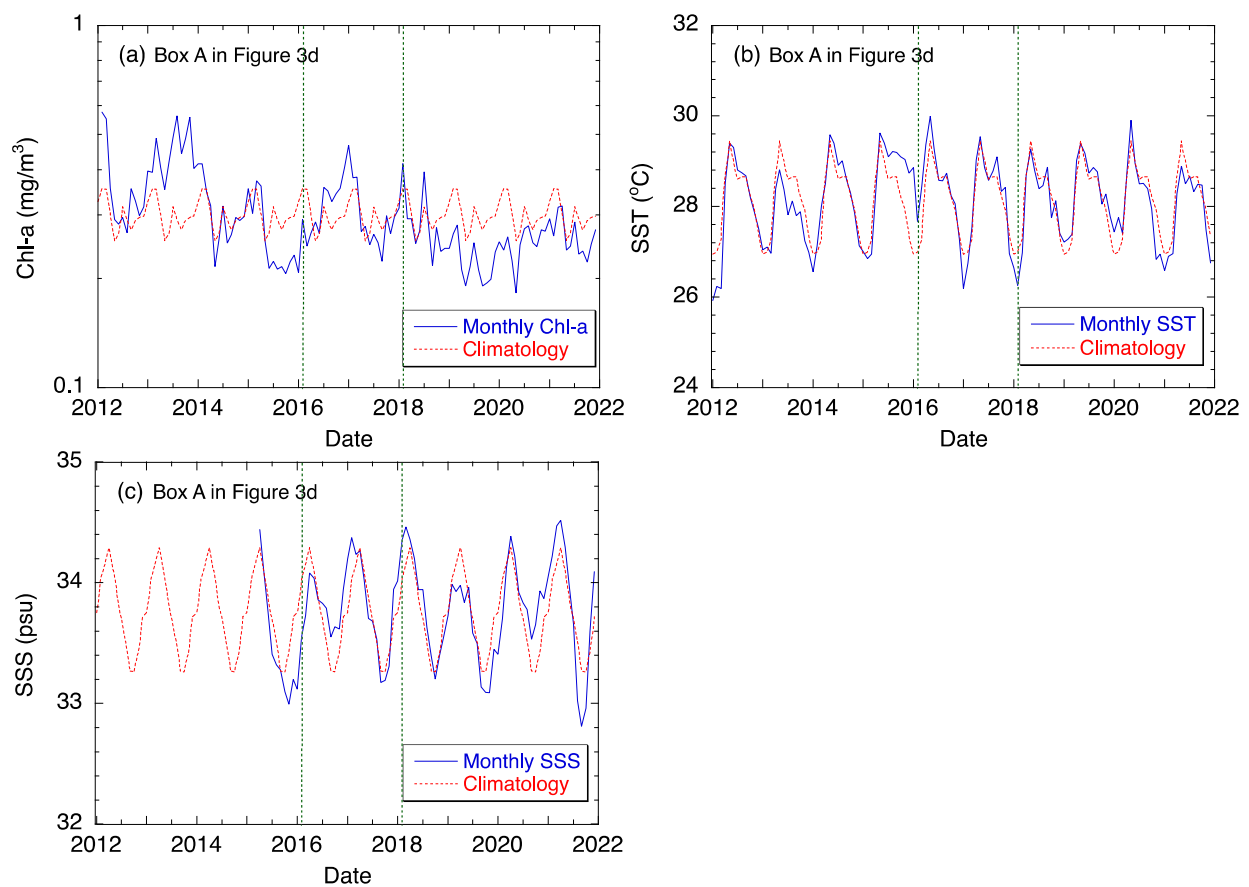


Figure 6. Temporal variations in Box A in Figure 3d from 2012 to 2021 in the CRTD region for (a) Chl-a, (b) SST, and (c) SSS. The vertical green color lines in plots mark the months of February 2016 and February 2018 for further analysis.

In comparison to the Chl-a variation between 2012 and 2021, the SST values in Box A show that the interannual change was less significant than the seasonal SST change (Figure 6b). The 10-year monthly mean SST values show that it peaked at $29.44 \text{ }^\circ\text{C}$ in May and was at its lowest at $26.94 \text{ }^\circ\text{C}$ in January. Even though the seasonal SST change was dominant, the interannual SST variability was also not negligible in the CRTD region. In 2013, the monthly SST values in Box A were $\sim 0.5\text{--}1.0 \text{ }^\circ\text{C}$ lower than the corresponding 10-year monthly mean SST values. In the period between the spring of 2015 and the spring of 2016, the difference in the monthly SST and the corresponding 10-year monthly mean SST in Box A could be over $\sim 1.0 \text{ }^\circ\text{C}$. In the period after early 2018, the monthly SST generally matched well with the corresponding 10-year monthly mean SST.

Even though SSS observations from SMAP only started in April 2015, the seasonal and interannual variability in SSS in Box A are evident (Figure 6c). Similar to the SST

changes, the seasonal SSS change was significant with 8-year monthly mean SSS ranging between 33.26 psu in October and 34.29 psu in April. The interannual SSS variability was also noticeable in the CRTD region. Specifically, the SSS anomaly as the difference between the monthly SSS and the corresponding 8-year monthly mean SSS changed from +0.48 psu in February 2016 to −0.37 psu in October 2016. In September 2021, the SSS in Box A reached the lowest value of 32.81 psu.

The CRTD region is highly variable not only for Chl-a, SST, and SSS, as shown in Figure 6a–c, but also for the locations and areal coverage of these properties. Figure 7a shows the core location of the CRTD identified as having the lowest SST in February between 2012 and 2021. Clearly, the locations of the core CRTD spread in a wide region over these ten years. The core CRTD were situated around [87.5°W, 10.5°N] for five times in this 10-year period. In these 10 years, the core location of the CRTD even reached much farther offshore at around [89.0°W, 9.0°N] in February 2016.

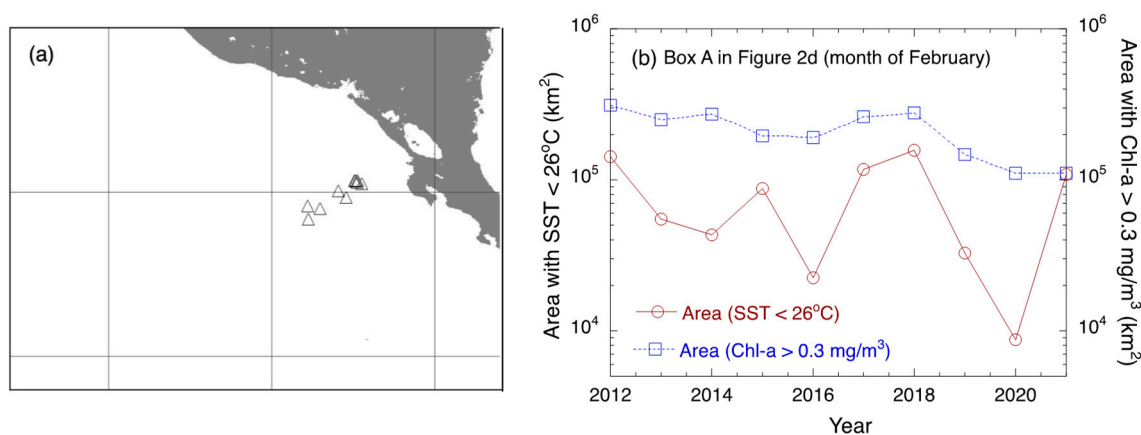


Figure 7. (a) Locations of the lowest SST and (b) coverage area with SST < 26 °C (scale noted in left) and coverage area with Chl-a > 0.3 mg/m³ (scale noted in right) in each February between 2012 and 2021. The core locations of the CRTD are marked in triangles in (a).

The spatial areal coverages and extensions of the CRTD were also highly variable between 2012 and 2021 (Figure 7b). In Box A, we also calculated the coverage areas of low SST (<26 °C) and elevated Chl-a (>0.3 mg/m³). Using the SST < 26 °C as the criteria, the spatial coverage ranged from less than 10,000 km² in February 2020 to 157,000 km² in February 2018. On the other hand, the change in the area with Chl-a > 0.3 mg/m³ was less significant than the interannual change in area for SST < 26 °C. In February 2012, the area for Chl-a > 0.3 mg/m³ was 312,000 km², while it was 112,000 km² in February 2020. It is also noted that the interannual changes in area coverage of the low SST and elevated Chl-a in February 2012–2021 did not always show the same variability as the interannual changes in SST and Chl-a in February 2012–2021, as shown in Figure 6a,b. This suggests that both the magnitudes and spatial distributions of SST and Chl-a play important roles in determining the mean monthly values of SST and Chl-a in Box A.

Figure 6 only shows the temporal variations in Chl-a, SST, and SSS in the CRTD region for the period of 2012–2021. Since the SST change essentially reflects the CRTD water property changes, we chose February 2016 and February 2018, as marked in Figure 6, to study the spatial distributions of these physical and biological properties in different scenarios of the CRTD. In February 2016, the SST values were about 1 °C higher than the corresponding 10-year mean SST in this same month in Box A. In contrast, the SST values in February 2018 were about 0.7 °C lower than the corresponding 10-year mean SST in February in Box A. With these two opposite situations in the CRTD region, the interannual variation in the spatial distributions of Chl-a, SST, and SSS can be characterized and examined.

As references, the maps of the climatology for Chl-a (Figure 8a), SST (Figure 8b), and SSS (Figure 8c) in February are produced. In comparison to the climatology (Figure 3d–f)

and seasonal climatology values (Figure 5), the features of elevated Chl-a (Figure 8a), SSS (Figure 8c), and depressed SST (Figure 8b) were more pronounced in this month. In February 2016, the Chl-a values (Figure 8d) in the entire CRTD region were less than those of the February climatology Chl-a (Figure 8a). The enhanced Chl-a pattern only reached around [92.5°W, 7.5°N] offshore in February 2016, while it extended much farther offshore in the February climatology Chl-a map. The maximal Chl-a values in February were 0.4–0.5 mg/m³, which were much lower than those in the February climatology Chl-a map.

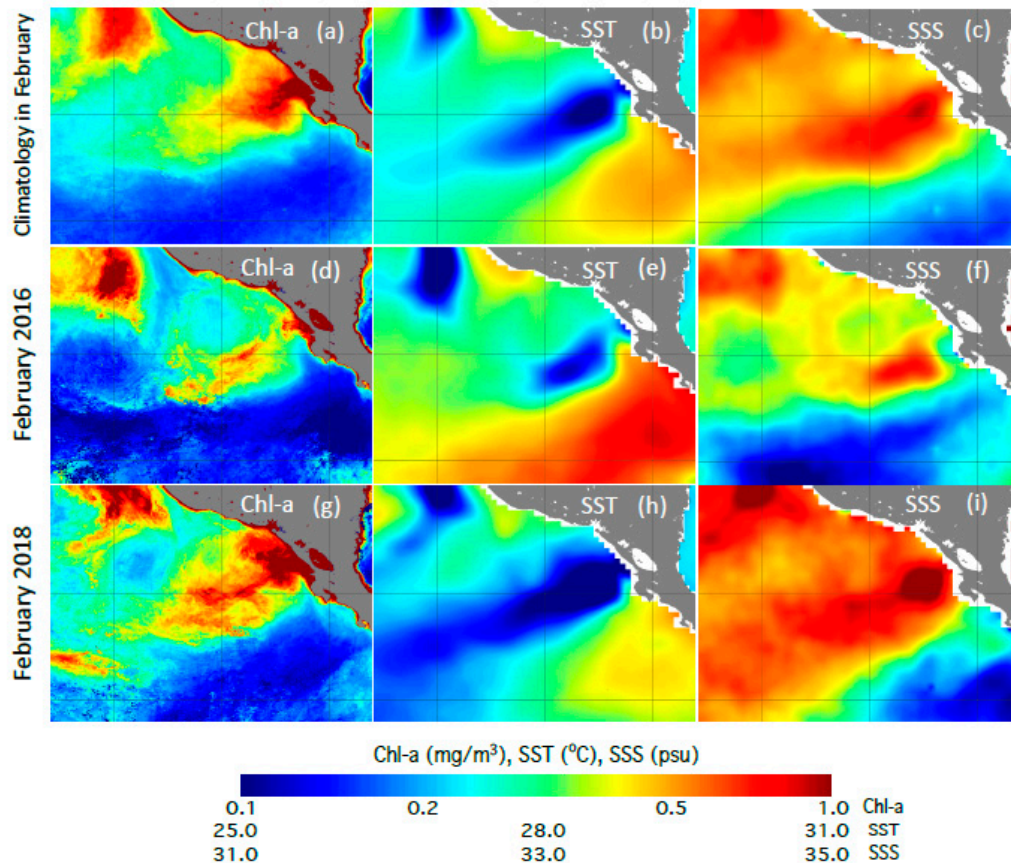


Figure 8. Comparisons of the specific water property parameter of the February climatology, February 2016, and February 2018 for (a,d,g) Chl-a, (b,e,h) SST, and (c,f,i) SSS.

In February 2016, the reduced SST values in the CRTD region (Figure 8e) were less significant than those of the February SST climatology (Figure 8b) for both the areal coverage and SST magnitude. The area with an SST < 26 °C in February 2016 was only one-quarter of the February SST climatology area. The SST values in February 2016 were generally ~1 °C higher than those of the February climatology SST. Different from SST, SSS in February 2016 (Figure 8f) showed a broad decrease in comparison to the same month SSS climatology (Figure 8c). Unlike the SSS climatology, the enhanced SSS in February 2016 only covered a small portion of the enhanced SSS in the February SSS climatology.

The sea surface features of the CRTD region in February 2018 represent the opposite situation to those in February 2016. For Chl-a, the enhanced Chl-a in the CRTD region further extended offshore and the magnitude of Chl-a in the large area exceeded ~1.0 mg/m³ (Figure 8g). The signature of lower SST in the CRTD region in February 2018 (Figure 8h) was more evident than that in the February climatology (Figure 8b). The area with SST < 25 °C in February 2018 was much larger than that in the February SST climatology. SSS over the CRTD region in February 2018 (Figure 8i) was more enhanced than SSS in the February SSS climatology (Figure 8c). In comparison to SSS in February 2016 (Figure 8f), SSS in February 2018 was over ~1.0 psu higher in large parts of the CRTD region.

Table 1 further quantifies Chl-a, SST, and SSS in Box A in February 2016 and 2018, as well as the corresponding climatology values. The mean climatology value of Chl-a was 0.441 mg/m³. It dropped to 0.322 mg/m³ in February 2016 and increased to 0.490 mg/m³ in February 2018. On the other hand, the mean SST increased to 27.67 °C in February 2016, while it decreased to 26.26 °C in February 2018. The mean SSS in Box A also showed an overall decrease from a climatology value of 34.09 psu to 33.5 psu in February 2016, while it increased to 34.35 psu in February 2018.

Table 1. Statistics of ocean properties (mean and median of Chl-a, SST, and SSS) in Box A for February climatology (Feb. Clim.) and February in 2016 and 2018.

Parameter	Feb. Clim. Mean	Feb. Clim. Median	Feb. 2016 Mean	Feb. 2016 Median	Feb. 2018 Mean	Feb. 2018 Median
Chl-a (mg/m ³)	0.441	0.364	0.322	0.291	0.490	0.417
SST (°C)	26.99	27.14	27.67	27.87	26.25	26.32
SSS (psu)	34.09	34.04	33.55	33.51	34.35	34.33

3.4. Subsurface Variability in the CRTD Region

Figures 5–8 show the sea surface features of Chl-a, SST, and SSS in the CRTD region. To further understand the variability in these properties, physical processes, and the driving mechanisms for the sea surface features, the in situ measurements at the TAO_95W_08N station were examined and analyzed. This station is the northeast most station of all the TAO stations in the tropical Pacific and is located in the CRTD region (Figure 3d). Thus, it provides an insightful assessment of the subsurface ocean dynamics that drives the seasonal and interannual variability in Chl-a, SST, and SSS in the CRTD region.

Due to the frequent measurement gaps at the TAO_95W_08N station, we evaluated the measurements between 2015 and 2019. At this station, the variability in SST showed similar SST variability in Box A, as shown in Figure 6b. Specifically, the SST values were over ~1 °C higher than the climatology SST in February 2016. On the other hand, it was ~1 °C lower than the climatology SST in February 2018 (Figure 9a). This suggested that the subsurface features at this station was representative for the entire CRTD region, and the dynamics at this station could be used to study the subsurface features of the CRTD region to further understand the physical, optical, biological, and biogeochemical processes that drive the variability in these sea surface ocean properties.

Figure 9b shows that the SSS variability at this station was also similar to the SSS variability in Box A (Figure 6c) between 2015 and 2019. In February 2016, the SSS values were ~1 psu lower than the climatology SSS at this station, while they were almost the same as the climatology in February following a quick increase from about 1 psu lower than the climatology SSS in September 2017. In May 2018, it reached a value 0.5 psu higher than the corresponding climatology SSS.

The variability in the 20 °C isothermal depth at this station showed significant interannual variability (Figure 9c), ranging from about 86 m of depth to 25 m of depth. In February 2016, the 20 °C isothermal depth deepened to 85 m with the increase in SST and the decrease in SSS at the station. In February 2018, the isothermal depth shoaled to 25 m with the decreasing SST and increasing SSS at the station. Corresponding to the thermocline dynamics as shown in Figure 9c, dynamic height at the station also changed significantly between 2015 and 2019. Specifically, the dynamic height was 115 cm in February 2016 in comparison to 85 cm in February 2018. The variability in the 20 isothermal depth and the dynamic height between 2015 and 2019 evidently showed that the subsurface dynamics at the CRTD region indeed was the driving force for the sea surface variability in Chl-a, SST, and SSS.

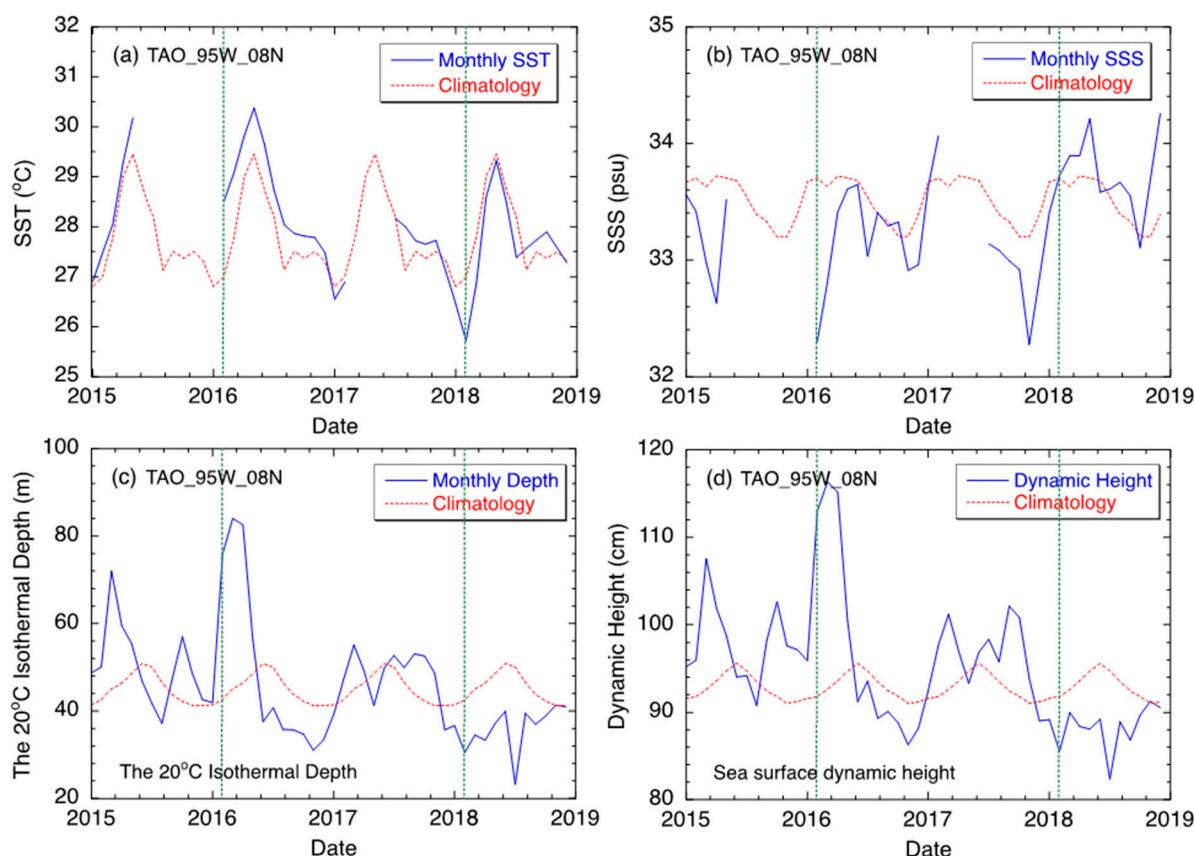


Figure 9. Monthly time series at the station TAO_95W_08N between 2015 and 2018 for (a) SST, (b) SSS, (c) the 20 °C isothermal depth, and (d) sea surface dynamic height. Note that the corresponding monthly climatology for each parameter is also shown for the months of February 2016 and February 2018 marked in each plot.

Figure 10 further shows the temperature in the upper 200 m depth at this station between 2015 and 2018. At the station, there were no salinity profile measurements in this period. In general, the 20 °C isothermal depth was located at ~40–50 m of depth, as shown for the climatology 20 °C isothermal depth in Figure 9c. The temperature quickly dropped from 24 °C to 16 °C across a ~20 m thick thermocline layer in this period. In February 2016, the temperature at this station spiked in the upper 150 m. The mixed-layer depth with temperature at 28 °C was about 50 m, and water temperature was 20 °C at 100 m of depth in comparison with 13–14 °C at this depth in the other time periods. As a comparison, the temperature profile presented lower values, a thin mixed layer, and a shoaling thermocline depth in February 2018. The thermocline depth shoaled to 25 m, while normally, it ranged from 40 to 50 m in this period. In fact, the mixed layer was disrupted and became very thin. The difference in the temperature profile in February 2016 and that in February 2018 manifested that the sea surface features of Chl-a, SST, and SSS as observed by satellite remote sensing indeed were intrinsically linked to the subsurface changes in these ocean properties. Indeed, these subsurface temperature variability in Figure 10 provides us with an insight on the ocean dynamics and processes that drive the change in the sea surface features in the CRTD region.

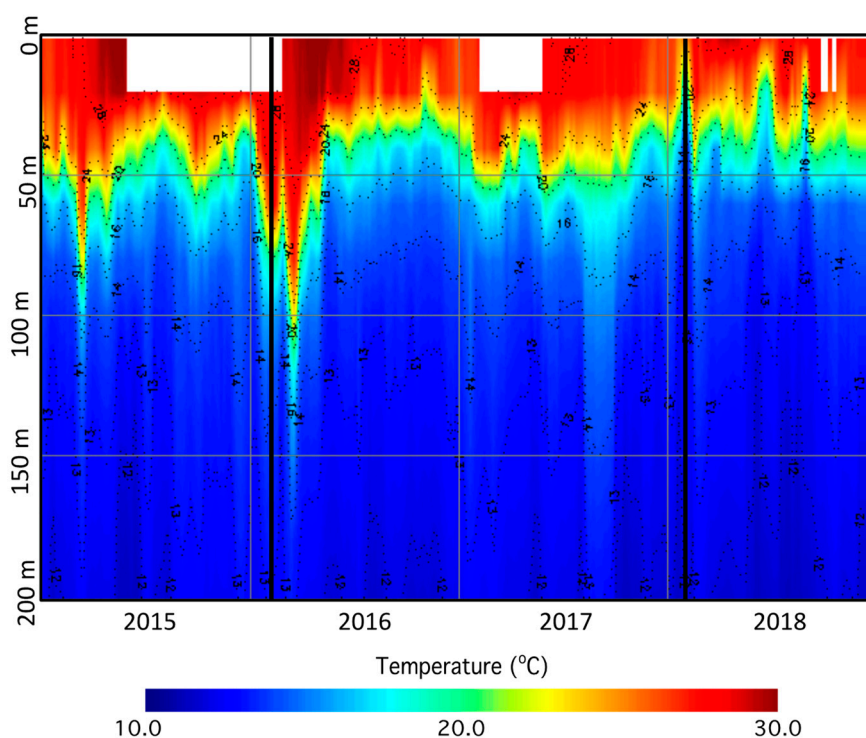


Figure 10. Temperature in the upper 200 m column at the station TAO_95W_08N between 2015 and 2018. The month of February 2016 and the month of February 2018 are also noted.

4. Discussion

4.1. Linkage among Chl-a, SST, and SSS Features

In comparison to various studies that used short-term satellite ocean color data (usually less than a couple of years) to understand the biological variability in the CRTD region, in this study, 10-year satellite ocean color observations are used to derive the seasonal climatology of Chl-a and its interannual variability. Furthermore, satellite SSS values are used to quantify the seasonal and interannual variability for the first time in the CRTD region. Long-term records of satellite ocean color, SST, and the new usage of SSS data provide us with a good opportunity to have an insight into the co-variation in the sea surface properties in the region.

The sea surface features of Chl-a, SST, and SSS are linked among them since both the seasonal and interannual features of Chl-a, SST, and SSS are driven by the same ocean processes such as upwelling, trade winds, the migration of the ITCZ, etc. Recent studies show that the variations in the Chl-a, SST, and SSS are linked in the Arabian Sea and equatorial Indian Ocean [54]. For the seasonal features in the CRTD, the spatial pattern of the elevated Chl-a generally matches well with the depressed SST and enhanced SSS as shown in Figure 5. In the CRTD region, both the salinity and nutrients such as nitrate and phosphate concentrations increase with the water depth [55]. This implies that the seasonal ocean processes such as the upwelling bring up the high-nutrient and high-salinity subsurface water to the surface mixed-layer, leading to the enhanced SSS and the higher levels of nutrients which also trigger the higher degree of algal growth in the CRTD region.

The interannual variability in Chl-a, SST, and SSS also generally presented a similar co-variability. The comparisons of the monthly Chl-a, SST, and SSS with their corresponding climatology values in Figures 6 and 8 showed that negative SST anomaly in 2013 coincided with the positive Chl-a, while the positive SST anomaly occurred with suppressed Chl-a and the negative SSS anomaly in the period between 2015 and early 2016 (Figure 6). Figure 9c shows the mixed-layer depth became thicker and thermocline depth deepened in the period between 2015 and early 2016 in comparison to those in other years. This suggests that higher SST and lower SSS can be attributed to the weakened upwelling. The

weaker upwelling also led to a deficiency in the nutrients for the phytoplankton growth, and consequently, Chl-a, in this period, was lower than the climatology Chl-a over the CRTD region. The observation agrees with the modelling results, showing that nutrient-rich waters are pumped up to the ocean surface-layer through vertical mixing. In fact, ocean upwelling plays a major role in ocean production and productivity. Therefore, thermocline depth is strongly connected to the seasonal variability in surface Chl-a [12,16].

4.2. ENSO Impact on Chl-a, SST, and SSS Features

ENSO is the major driver for the interannual variability in Chl-a, SST, and SSS. In the period from 2012 to 2021, there were four El Niño and La Niña events from the multivariate ENSO index (MEI) (<https://psl.noaa.gov/enso/mei/>; accessed on 10 April 2024) [56,57]. Specifically, we identified the La Niña event in 2013 with the lowest MEI at -1.2 , the El Niño event with the highest MEI of 2.2 in 2015–2016, the La Niña event in 2017–2018 the lowest MEI at -1.3 , and the La Niña event in 2020–2021 with the lowest MEI at -1.5 .

For the La Niña event in 2013 and El Niño in 2015–2016, the interannual variability in Chl-a and SST followed the similar variability patterns of Chl-a and SST in the other La Niña and El Niño events as reported and modelled [16]. During the La Niña phase with a cold SST anomaly in 2013, Chl-a was considerably higher than that in other years, while Chl-a values were remarkably lower than those in other years with a warm SST anomaly during the El Niño event in 2015–2016.

During the La Niña event in 2017–2018, the SST values were moderately lower than those of the climatology SST (Figure 6b), and the Chl-a values in Box A were higher than those of the corresponding climatology Chl-a for most of the time of the La Niña duration. As an example, the Chl-a map in February 2018 shows the spatial coverage of high Chl-a expanded and its magnitude became even higher (Figure 8). Furthermore, the time series of SSS (Figure 6c) and the SSS map (Figure 8) also show that the ENSO event impact was significant with depressed SSS in the 2015–2016 El Niño event and enhanced SSS in the 2017–2018 La Niña event. The depressed SSS during the El Niño events in 2013 were also expected, although there were no SSS satellite measurements at that time.

Unlike normally depressed SST with enhanced Chl-a and SSS during La Niña events, as shown in Figure 8g–i in February 2018, it is interesting to find that the corresponding changes in lower SST and enhanced Chl-a and SSS in the La Niña event in 2020–2021 did not happen. Figure 11 shows the maps of Chl-a (Figure 11a), SST (Figure 11b), and SSS (Figure 11c) in February 2021 in the CRTD region. Compared to the climatology Chl-a (Figure 8a), SST (Figure 8b), and SSS (Figure 8c), Chl-a was not elevated in February 2021 (Figure 11a). The SST pattern in February 2021 (Figure 11b) was similar to the climatology SST (Figure 8b), and SSS in February 2021 (Figure 11c) was slightly higher than the climatology SSS (Figure 8c).

In February 2021, the La Niña event lasted nine months since June 2020, with the $MEI < -0.5$, and in fact, the MEI values were -1.2 , -0.9 , and -0.8 in January, February, and March of 2021, respectively. In January, February, and March 2018, the MEI values were -0.8 , -0.7 , and -0.8 . Even though the La Niña in February 2018 was weaker than the La Niña in February 2021 in terms of the MEI values, changes in Chl-a (Figure 8g), SST (Figure 8h), and SSS (Figure 8i) in February 2018 were actually stronger than those in February 2021 (Figure 11a–c) in comparison to the climatology Chl-a, SST, and SSS in February (Figure 8a–c). The anomalies of Chl-a (Figure 11d), SST (Figure 11e), and SSS (Figure 11f) clearly show the changes in the sea surface features in the 2020–2021 La Niña event. In the CRTD coastal region, Chl-a (Figure 11a) dropped significantly with a positive SST anomaly (Figure 11e). The moderate Chl-a increase, SST drop, and higher SSS were actually located further south between $5^{\circ}N$ and $8^{\circ}N$.

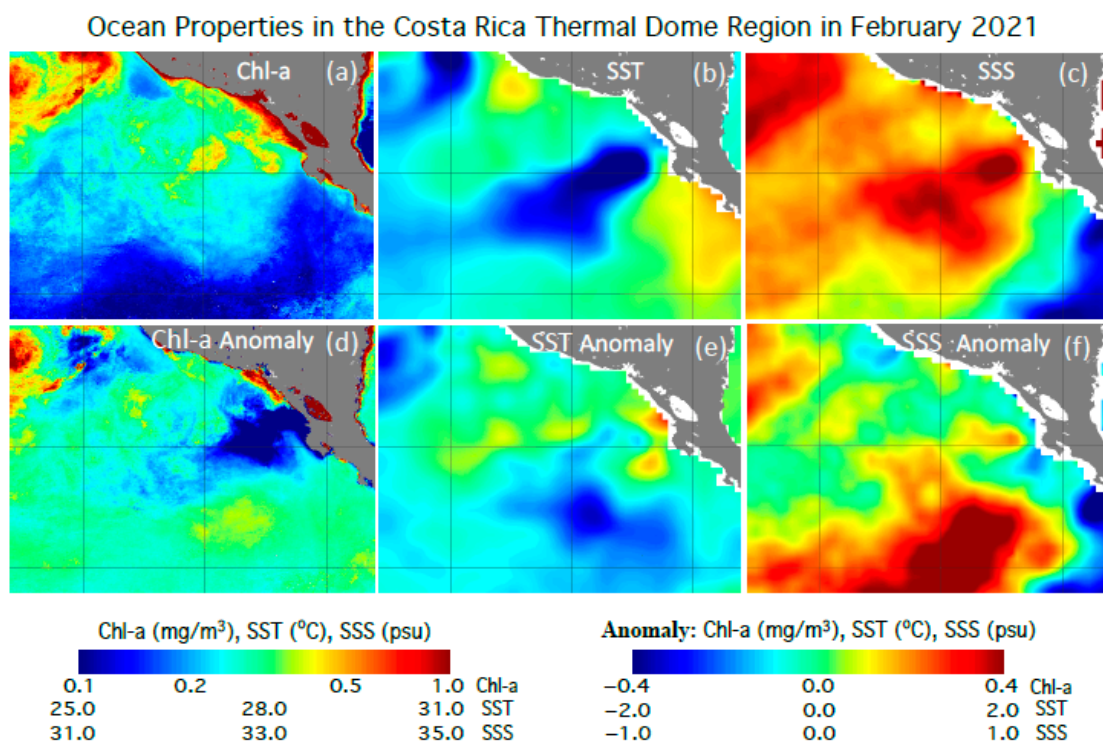


Figure 11. The maps of sea surface properties in February 2021 for (a) Chl-a, (b) SST, (c) SSS, (d) Chl-a anomaly, (e) SST anomaly, and (f) SSS anomaly.

The sea surface features in the CTRD region, in 2020–2021, apparently were inconsistent with the observations and modeling results for the impact of ENSO [16]. It was also different from the Chl-a, SST, and SSS features in the 2017–2018 La Niña event. An examination of SST in the equatorial Pacific in these 10 years shows that the significantly negative SST anomaly in the 2013 La Niña and positive SST anomalies of El Niño in 2015–2016 were located in the eastern equatorial Pacific, while the SST anomaly in the 2020–2021 La Niña event was across the eastern and central equatorial Pacific. In fact, the SST anomaly in the 2020–2021 La Niña was significantly lower than those in the 2013 and 2017–2018 La Niña events.

The traditional eastern Pacific (EP) ENSO and central Pacific (CP) ENSO are the two different modes of ENSO with contrasting SST anomaly patterns in the equatorial Pacific [58–60]. The SST patterns in the equatorial Pacific evidently showed that the La Niña events in 2013 and 2017–2018 were EP La Niña events, while the La Niña event in 2020–2021 was a CP La Niña event. The central Pacific ENSO has most of its surface wind, SST, and subsurface anomalies confined in the central Pacific region instead of East Pacific, and it is less related to the thermocline variations [58]. This implies that the coastal and open ocean upwelling in the CRTD region in the 2020–2021 La Niña event was not as strong as the upwelling in the 2013 and 2017–2018 La Niña events, even though the MEI was even more negative and lasted longer in the 2020–2021 La Niña event. Consequently, the surface nutrient levels were not elevated significantly in the 2020–2021 La Niña event due to the dampened upwelling. Therefore, no enhanced Chl-a, as shown in Figure 6a, was observed in the 2020–2021 La Niña event.

5. Conclusions

Using VIIRS-SNPP satellite ocean color products, SST from GODAS and SSS observations from SMAP, we characterized and quantified the sea surface features of $nL_w(\lambda)$, Chl-a, SST, and SSS since 2012 in the CRTD region. The climatology of SST, SSS, and ocean color properties were provided. In comparison to the in situ-based SST and SSS climatology, the satellite-derived SST and SSS climatology data had a fine resolution and provided more

details in terms of spatial variability. On the other hand, the mission-long climatology and their variability for the ocean color properties, e.g., Chl-a, were produced for the first time in the CRTD region.

The seasonal and interannual variability in these sea surface features were computed. The co-variations in these ocean properties in the CRTD region were examined and identified. The linkage and correlation between the interannual variability in these sea surface features were reported, and the impact of the ENSO events on the equatorial Pacific Ocean was also addressed. The driving force for the interannual variability was further explored with the in situ measurements in the subsurface layer.

The seasonal maps of Chl-a, SST, and SSS in the CRTD region showed that these ocean properties were linked. The elevated Chl-a matched the depressed SST and enhanced SSS in the climatology seasonal maps of these three properties. This reflected that the physical driving force, i.e., upwelling, trade winds, and the migration of the ITCZ, was the same for these sea surface properties. On the other hand, the similarity and colocations of seasonal Chl-a, SST, and SSS provided evidence that the cold high-salinity water brought to the sea surface was high-nutrient water; thus, nutrient supplies enhanced the algal growth in the CRTD region.

The interannual variability in Chl-a, SST, and SSS also showed that these three sea surface properties were consistent among them. The positive Chl-a anomaly generally occurred with the depressed SST and enhanced SSS and vice versa. The subsurface dynamics followed the sea surface dynamics of these properties. The 20 °C isothermal depth deepened with enhanced SST and depressed Chl-a and SSS. In comparison, it shoaled to shallow depths when SST was depressed and Chl-a and SSS were elevated.

In the 10-year period, there occurred four major ENSO events. Three of them resulted in significantly biological variability, i.e., lower-than-normal Chl-a, was observed during the El Niño event and higher-than-normal Chl-a during the La Niña event in the CRTD region. This is consistent with the previous studies. However, no significant enhancement of Chl-a was observed in the region during the 2020–2021 La Niña event. This was attributed to the fact that the 2020–2021 La Niña event was a central Pacific ENSO event, while the other three were eastern Pacific ENSO events. For the future research, a diagnostic analysis of wind curl, wind anomalies, or the upwelling index to discern the oceanic responses to the two types of ENSO events is necessary to better understand the interactions between the ocean physical, biological, and biogeochemical processes in the CRTD region.

Author Contributions: Conceptualization, W.S.; Methodology, W.S.; Investigation, W.S.; Writing—original draft, W.S.; Writing—review & editing, M.W.; Project administration, M.W.; Funding acquisition, M.W. All authors have read and agreed to the published version of the manuscript.

Funding: This research was supported by the Joint Polar Satellite System (JPSS) funding.

Data Availability Statement: VIIRS global ocean color product data can be found at the NOAA Ocean Color Team website (<https://www.star.nesdis.noaa.gov/sod/mecb/color/>, accessed on 10 April 2024). The SMAP SSS data were acquired from the Jet Propulsion Laboratory (JPL) Physical Oceanography Distributed Active Archive Center (PODAAC) (<https://doi.org/10.5067/SMP50-3TPCS>, accessed on 10 April 2024). The TAO data were acquired from the NOAA Pacific Marine Environmental Laboratory (PMEL) (<https://www.pmel.noaa.gov/gtmba/>, accessed on 10 April 2024).

Acknowledgments: We thank three anonymous reviewers for their useful comments. The scientific results and conclusions, as well as any views or opinions expressed herein, are those of the author(s) and do not necessarily reflect those of the NOAA or the Department of Commerce.

Conflicts of Interest: The authors declare no conflict of interest.

References

1. Cromwell, T. Thermocline topography, horizontal currents and “ridging” in the eastern tropical Pacific. *Bull. Inter-Am. Trop. Tuna Comm.* **1958**, *111*, 135–164.
2. Wyrtki, K. Upwelling in the Costa Rica Dome. *Fish. Bull.* **1964**, *63*, 355–372.
3. Fiedler, P.C. The annual cycle and biological effects of the Costa Rica Dome. *Deep-Sea Res. Part I* **2002**, *49*, 321–338. [[CrossRef](#)]

4. Jimenez, J. *The Costa Rica Thermic Dome*; MarViva: Romsey, UK, 2017; p. 55.
5. Wyrski, K.; Kendall, R. Transports of the Pacific Equatorial Countercurrent. *J. Geophys. Res.* **1967**, *72*, 2073–2076. [[CrossRef](#)]
6. McPhaden, M.J. Monthly period oscillations in the Pacific North Equatorial Countercurrent. *J. Geophys. Res. Oceans* **1996**, *101*, 6337–6359. [[CrossRef](#)]
7. Zhao, J.; Li, Y.L.; Wang, F. Dynamical responses of the west Pacific North Equatorial Countercurrent (NECC) system to El Nino events. *J. Geophys. Res. Oceans* **2013**, *118*, 2828–2844. [[CrossRef](#)]
8. Kessler, W.S. The circulation of the eastern tropical Pacific: A review. *Prog. Oceanogr.* **2006**, *69*, 181–217. [[CrossRef](#)]
9. Schonau, M.C.; Rudnick, D.L. Glider observations of the North Equatorial Current in the western tropical Pacific. *J. Geophys. Res. Oceans* **2015**, *120*, 3586–3605. [[CrossRef](#)]
10. Hofmann, E.E.; Busalacchi, A.J.; O'Brien, J.J. Wind Generation of the Costa-Rica Dome. *Science* **1981**, *214*, 552–554. [[CrossRef](#)]
11. Umatani, S.; Yamagata, T. Response of the Eastern Tropical Pacific to Meridional Migration of the ITCZ—The Generation of the Costa-Rica Dome. *J. Phys. Ocean.* **1991**, *21*, 346–363. [[CrossRef](#)]
12. Sasai, Y.; Sasaki, H.; Sasaoka, K.; Ishida, A.; Yamanaka, Y. Marine ecosystem simulation in the eastern tropical Pacific with a global eddy resolving coupled physical-biological model. *Geophys. Res. Lett.* **2007**, *34*, L23601. [[CrossRef](#)]
13. Broenkow, W.W. The distribution of nutrients in the Costa Rica dome in the eastern tropical Pacific ocean. *Limnol. Oceanogr.* **1965**, *10*, 40–52. [[CrossRef](#)]
14. McClain, C.R.; Christian, J.R.; Signorini, S.R.; Lewis, M.R.; Asanuma, I.; Turk, D.; Dupouy-Douchement, C. Satellite ocean-color observations of the tropical Pacific Ocean. *Deep-Sea Res. Part II* **2002**, *49*, 2533–2560. [[CrossRef](#)]
15. Fiedler, P.C.; Philbrick, V.; Chavez, F.P. Oceanic Upwelling and Productivity in the Eastern Tropical Pacific. *Limnol. Oceanogr.* **1991**, *36*, 1834–1850. [[CrossRef](#)]
16. Sasai, Y.; Richards, K.J.; Ishida, A.; Sasaki, H. Spatial and temporal variabilities of the chlorophyll distribution in the northeastern tropical Pacific: The impact of physical processes on seasonal and interannual time scales. *J. Mar. Syst.* **2012**, *96–97*, 24–31. [[CrossRef](#)]
17. Pennington, J.T.; Mahoney, K.L.; Kuwahara, V.S.; Kolber, D.D.; Calienes, R.; Chavez, F.P. Primary production in the eastern tropical Pacific: A review. *Prog. Oceanogr.* **2006**, *69*, 285–317. [[CrossRef](#)]
18. Barber, R.T.; Chavez, F.P. Regulation of Primary Productivity Rate in the Equatorial Pacific. *Limnol. Oceanogr.* **1991**, *36*, 1803–1815. [[CrossRef](#)]
19. Landry, M.R.; Selph, K.E.; Decima, M.; Gutierrez-Rodriguez, A.; Stukel, M.R.; Taylor, A.G.; Pasulka, A.L. Phytoplankton production and grazing balances in the Costa Rica Dome. *J. Plankton Res.* **2016**, *38*, 366–379. [[CrossRef](#)] [[PubMed](#)]
20. Minas, H.J.; Minas, M. Net Community Production in High Nutrient-Low Chlorophyll Waters of the Tropical and Antarctic Oceans—Grazing Vs Iron Hypothesis. *Ocean. Acta* **1992**, *15*, 145–162.
21. Fernandez-Alamo, M.A.; Farber-Lorda, J. Zooplankton and the oceanography of the eastern tropical Pacific: A review. *Prog. Oceanogr.* **2006**, *69*, 318–359. [[CrossRef](#)]
22. Sameoto, D.; Guglielmo, L.; Lewis, M.K. Day Night Vertical-Distribution of Euphausiids in the Eastern Tropical Pacific. *Mar. Biol.* **1987**, *96*, 235–245. [[CrossRef](#)]
23. Evseenko, S.A.; Shtaut, M.I. On the Species Composition and Distribution of Ichthyoplankton and Micronekton in the Costa Rica Dome and Adjacent Areas of the Tropical Eastern Pacific. *J. Ichthyol.* **2005**, *45*, 512–524.
24. Joseph, J. The Tuna-Dolphin Controversy in the Eastern Pacific-Ocean—Biological, Economic, and Political Impacts. *Ocean. Dev. Int. Law.* **1994**, *25*, 1–30. [[CrossRef](#)]
25. De Anda-Montanez, J.A.; Amador-Buenrostro, A.; Martinez-Aguilar, S.; Muhlia-Almazan, A. Spatial analysis of yellowfin tuna (*Thunnus albacares*) catch rate and its relation to El Nino and La Nina events in the eastern tropical Pacific. *Deep-Sea Res. Part II* **2004**, *51*, 575–586. [[CrossRef](#)]
26. Behringer, D.W.; Ji, M.; Leetmaa, A. An improved coupled model for ENSO prediction and implications for ocean initialization. Part I: The Ocean Data Assimilation System. *Mon. Weather. Rev.* **1998**, *126*, 1013–1021. [[CrossRef](#)]
27. Derber, J.; Rosati, A. A Global Oceanic Data Assimilation System. *J. Phys. Ocean.* **1989**, *19*, 1333–1347. [[CrossRef](#)]
28. O'Neill, P.; Entekhabi, D.; Njoku, E.; Kellogg, K. The Nasa Soil Moisture Active Passive (Smapp) Mission: Overview. In Proceedings of the 2010 IEEE International Geoscience and Remote Sensing Symposium, Honolulu, HI, USA, 25–30 July 2010; pp. 3236–3239. [[CrossRef](#)]
29. Salomonson, V.V.; Barnes, W.L.; Maymon, P.W.; Montgomery, H.E.; Ostrow, H. Modis—Advanced Facility Instrument for Studies of the Earth as a System. *IEEE Trans. Geosci. Remote Sens.* **1989**, *27*, 145–153. [[CrossRef](#)]
30. Esaias, W.E.; Abbott, M.R.; Barton, I.; Brown, O.B.; Campbell, J.W.; Carder, K.L.; Clark, D.K.; Evans, R.H.; Hoge, F.E.; Gordon, H.R.; et al. An overview of MODIS capabilities for ocean science observations. *IEEE Trans. Geosci. Remote Sens.* **1998**, *36*, 1250–1265. [[CrossRef](#)]
31. Goldberg, M.D.; Kilcoyne, H.; Cikanek, H.; Mehta, A. Joint Polar Satellite System: The United States next generation civilian polar-orbiting environmental satellite system. *J. Geophys. Res. Atmos.* **2013**, *118*, 13463–13475. [[CrossRef](#)]
32. Wang, M.; Liu, X.; Tan, L.; Jiang, L.; Son, S.; Shi, W.; Rausch, K.; Voss, K. Impacts of VIIRS SDR performance on ocean color products. *J. Geophys. Res. Atmos.* **2013**, *118*, 10347–10360. [[CrossRef](#)]
33. Gordon, H.R.; Wang, M. Retrieval of Water-Leaving Radiance and Aerosol Optical-Thickness over the Oceans with SeaWiFS—A Preliminary Algorithm. *Appl. Opt.* **1994**, *33*, 443–452. [[CrossRef](#)] [[PubMed](#)]

34. Wang, M.; Shi, W. The NIR-SWIR combined atmospheric correction approach for MODIS ocean color data processing. *Opt. Expr.* **2007**, *15*, 15722–15733. [[CrossRef](#)] [[PubMed](#)]
35. Wang, M. Remote sensing of the ocean contributions from ultraviolet to near-infrared using the shortwave infrared bands: Simulations. *Appl. Opt.* **2007**, *46*, 1535–1547. [[CrossRef](#)]
36. McClain, C.R.; Feldman, G.C.; Hooker, S.B. An overview of the SeaWiFS project and strategies for producing a climate research quality global ocean bio-optical time series. *Deep-Sea Res. Part II* **2004**, *51*, 5–42. [[CrossRef](#)]
37. McClain, C.R. A Decade of Satellite Ocean Color Observations. *Annu. Rev. Mar. Sci.* **2009**, *1*, 19–42. [[CrossRef](#)] [[PubMed](#)]
38. Clark, D.K.; Gordon, H.R.; Voss, K.J.; Ge, Y.; Broenkow, W.; Trees, C. Validation of atmospheric correction over the oceans. *J. Geophys. Res.-Atmos.* **1997**, *102*, 17209–17217. [[CrossRef](#)]
39. Wang, M.; Shi, W.; Jiang, L.; Voss, K. NIR- and SWIR-based on-orbit vicarious calibrations for satellite ocean color sensors. *Opt. Expr.* **2016**, *24*, 20437–20453. [[CrossRef](#)]
40. Barnes, B.B.; Cannizzaro, J.P.; English, D.C.; Hu, C.M. Validation of VIIRS and MODIS reflectance data in coastal and oceanic waters: An assessment of methods. *Remote Sens. Environ.* **2019**, *220*, 110–123. [[CrossRef](#)]
41. Mikelsons, K.; Wang, M.H.; Jiang, L.D. Statistical evaluation of satellite ocean color data retrievals. *Remote Sens. Environ.* **2020**, *237*, 111601. [[CrossRef](#)]
42. Wang, M.; Shi, W.; Watanabe, W. Satellite-measured water properties in high altitude Lake Tahoe. *Water Res.* **2020**, *178*, 115839. [[CrossRef](#)]
43. Hu, C.; Lee, Z.; Franz, B. Chlorophyll a algorithms for oligotrophic oceans: A novel approach based on three-band reflectance difference. *J. Geophys. Res. Oceans* **2012**, *117*, C01011. [[CrossRef](#)]
44. Wang, M.; Son, S. VIIRS-derived chlorophyll-a using the ocean color index method. *Remote Sens. Environ.* **2016**, *182*, 141–149. [[CrossRef](#)]
45. O'Reilly, J.E.; Maritorena, S.; Mitchell, B.G.; Siegel, D.A.; Carder, K.L.; Garver, S.A.; Kahru, M.; McClain, C. Ocean color chlorophyll algorithms for SeaWiFS. *J. Geophys. Res. Oceans* **1998**, *103*, 24937–24953. [[CrossRef](#)]
46. O'Reilly, J.E.; Werdell, P.J. Chlorophyll algorithms for ocean color sensors-OC4, OC5 & OC6. *Remote Sens. Environ.* **2019**, *229*, 32–47. [[CrossRef](#)] [[PubMed](#)]
47. Ravichandran, M.; Behringer, D.; Sivareddy, S.; Girishkumar, M.S.; Chacko, N.; Harikumar, R. Evaluation of the Global Ocean Data Assimilation System at INCOIS: The Tropical Indian Ocean. *Ocean Model.* **2013**, *69*, 123–135. [[CrossRef](#)]
48. Behringer, D.W.; Xue, Y. Evaluation of the global ocean data assimilation system at NCEP: The Pacific Ocean. In Proceedings of the Eighth Symposium on Integrated Observing and Assimilation Systems for Atmosphere, Oceans, and Land Surface AMS 84th Annual Meeting, Seattle, WA, USA, 11–14 January 2004.
49. Fore, A.G.; Yueh, S.H.; Tang, W.Q.; Stiles, B.W.; Hayashi, A.K. Combined Active/Passive Retrievals of Ocean Vector Wind and Sea Surface Salinity With SMAP. *IEEE Trans. Geosci. Remote Sens.* **2016**, *54*, 7396–7404. [[CrossRef](#)]
50. Chan, S.K.; Bindlish, R.; O'Neill, P.E.; Njoku, E.; Jackson, T.; Colliander, A.; Chen, F.; Burgin, M.; Dunbar, S.; Piepmeier, J.; et al. Assessment of the SMAP Passive Soil Moisture Product. *IEEE Trans. Geosci. Remote Sens.* **2016**, *54*, 4994–5007. [[CrossRef](#)]
51. Tang, W.Q.; Fore, A.; Yueh, S.; Lee, T.; Hayashi, A.; Sanchez-Franks, A.; Martinez, J.; King, B.; Baranowski, D. Validating SMAP SSS with in situ measurements. *Remote Sens. Environ.* **2017**, *200*, 326–340. [[CrossRef](#)]
52. McPhaden, M.J. The Tropical Atmosphere Ocean Array Is Completed. *Bull. Am. Meteorol. Soc.* **1995**, *76*, 739–741. [[CrossRef](#)]
53. McPhaden, M.J.; Busalacchi, A.J.; Cheney, R.; Donguy, J.R.; Gage, K.S.; Halpern, D.; Ji, M.; Julian, P.; Meyers, G.; Mitchum, G.T.; et al. The tropical ocean global atmosphere observing system: A decade of progress. *J. Geophys. Res. Oceans* **1998**, *103*, 14169–14240. [[CrossRef](#)]
54. Shi, W.; Wang, M. Phytoplankton biomass dynamics in the Arabian Sea from VIIRS observations. *J. Mar. Syst.* **2022**, *227*, 103670. [[CrossRef](#)]
55. Garcia, H.E.; Weathers, K.W.; Paver, C.R.; Smolyar, I.; Boyer, T.P.; Locarnini, R.A.; Zweng, M.M.; Mishonov, A.V.; Baranova, O.K.; Seidov, D.; et al. *World Ocean Atlas 2018. Vol. 4: Dissolved Inorganic Nutrients (Phosphate, Nitrate and Nitrate+Nitrite, Silicate)*; NOAA Atlas NESDIS 84; NOAA: Silver Spring, MD, USA, 2019; p. 35.
56. Wolter, K. The Southern Oscillation in Surface Circulation and Climate over the Tropical Atlantic, Eastern Pacific, and Indian Oceans as Captured by Cluster-Analysis. *J. Clim. Appl. Meteorol.* **1987**, *26*, 540–558. [[CrossRef](#)]
57. Wolter, K.; Timlin, M.S. El Nino/Southern Oscillation behaviour since 1871 as diagnosed in an extended multivariate ENSO index (MEI.ext). *Int. J. Clim.* **2011**, *31*, 1074–1087. [[CrossRef](#)]
58. Kao, H.Y.; Yu, J.Y. Contrasting Eastern-Pacific and Central-Pacific Types of ENSO. *J. Clim.* **2009**, *22*, 615–632. [[CrossRef](#)]
59. Yu, J.Y.; Kim, S.T. Identification of Central-Pacific and Eastern-Pacific types of ENSO in CMIP3 models. *Geophys. Res. Lett.* **2010**, *37*, L15705. [[CrossRef](#)]
60. Jeng, H.; Ahn, J. A new method to classify ENSO events into eastern and central Pacific types. *Int. J. Climatol.* **2016**, *37*, 2193–2199. [[CrossRef](#)]

Disclaimer/Publisher's Note: The statements, opinions and data contained in all publications are solely those of the individual author(s) and contributor(s) and not of MDPI and/or the editor(s). MDPI and/or the editor(s) disclaim responsibility for any injury to people or property resulting from any ideas, methods, instructions or products referred to in the content.